scientific reports

Check for updates

OPEN

Purine-based chemical probe with HOMO switching for intracellular detection of mercury ions

Kamilė Boguševičienė[1,6], Justina Jovaišaitė[1,6]✉, Gediminas Jonusauskas[1,2]✉, Gediminas Kreiza[1], Aleksejs Burcevs[3], Zigfrīds Kapilinskis[3], Irina Novosjolova[3], Maris Turks[3], Li Er Hean[4], Han-Wei Chu[4], Huang-Tsung Chang[4,5] & Saulius Juršėnas[1]

The detailed photophysical characterization of 2-piperidinyl-6-triazolylpurine derivatives and their complexes with metal ions is presented. The studied compounds contain two electron donating units – piperidine and methoxyphenyl, while triazolyl-purine acts as an electron acceptor. These derivatives possess good fluorescence quantum yields in both aprotic and aqueous environments. All piperidine-triazole-purine compounds exhibited a fluorescence "turn-off" sensing behavior to different metal ions, including Hg^{2+}. We are discussing the changes in photophysical properties occurring upon complexation including switching between highest occupied molecular orbitals (HOMOs) of different electron donating units and the entire electron charge shift possibility in the complex with mercury ion. The sensing concept was further applied for newly synthesized water-soluble compounds, that demonstrated better selectivity toward Hg^{2+} in aqueous media. Further, the selected 2-piperidinyl-6-triazolylpurine water-soluble derivative was employed as a "turn-off" chemical probe for mercury ion detection in living cells.

Keywords Purine, Chemical probe, Mercury ion sensing, "Turn-off" fluorescence, HOMO switching, Mercury ion imaging

Purine is the most widely distributed nitrogen heterocycle in nature and can be regarded as a unique heterocyclic base with respect to diverse possibilities of its chemical modifications[1]. The exceptional biological activity of purine-based derivatives, including antitumor[2], antiviral[3,4], antibacterial[5], and antioxidant properties[6], encouraged its development towards medical applications[7,8]. Furthermore, additional characteristics, such as good biocompatibility, large π-conjugated plane and multiple readily available modification sites have raised scientific interest to develop multifunctional purine-based fluorescent materials[9–13]. Recently, there has been an increasing number of publications presenting the potential applications of these derivatives, including organic light emitting diodes (OLEDs)[14–17], information encryption and anti-counterfeiting[18], bioimaging[19,20], as well as optical probes for metal ion sensing[21,22], including heavy metals, such as cadmium (II)[23] or palladium (II)[24].

Mercury is one of the heavy metals continuously raising concern due to its non-biodegradable nature, high toxicity and harmful effects on living organisms. Inorganic Hg^{2+} can transform into methylmercury, which readily bioaccumulates in animals and plants[25]. This bioaccumulation can ultimately lead to methylmercury's entry into the human body, most commonly through the consumption of contaminated fish and seafood[26]. It has been noticed that small amounts of methylmercury can be traced in almost all humans, indicating its widespread occurrence in the environment[27,28], including crops or terrestrial ecosystems[29]. Exposure to high levels of methylmercury may cause serious health problems, such as damage and disorder of nervous, digestive and immune systems[27,30,31]. As a result, ongoing efforts are focused on developing real-time detection and monitoring techniques for mercury in food, environment and biological samples, including Hg^{2+} imaging in living cells[29,32].

Chemical metal ion detection via colorimetry or fluorimetry is a promising tool due to its simplicity, use of non-sophisticated equipment, quick, sensitive and selective detection and the absence of specific sample

[1]Institute of Photonics and Nanotechnology, Faculty of Physics, Vilnius University, Saulėtekis Av. 3, LT-10222 Vilnius, Lithuania. [2]Laboratoire Ondes Et Matière d'Aquitaine, UMR CNRS 5798, Bordeaux University, 351 Cours de La Libération, 33405 Talence, France. [3]Institute of Chemistry and Chemical Technology, Faculty of Natural Sciences and Technology, Riga Technical University, P. Valdena Str. 3, Riga LV-1048, Latvia. [4]Department of Biomedical Sciences, College of Medicine, Chang Gung University, Taoyuan 33302, Taiwan. [5]College of Pharmacy, Kaohsiung Medical University, Kaohsiung 80708, Taiwan. [6]Kamilė Boguševičienė and Justina Jovaišaitė contributed equally to this work. ✉email: justina.jovaisaite@ff.vu.lt; gediminas.jonusauskas@u-bordeaux.fr

pre-treatment[33,34]. The fast-evolving field of molecular sensor chemistry is closely connected to the versatility of organic compounds and possibility to govern photophysical properties upon chemosensor-analyte complexation[35]. On the other hand, it remains a challenging task to create water-soluble, biocompatible, non-toxic and well coordinating organic molecular sensors that could additionally penetrate cell membrane and expand the range of applications in biological systems[36,37]. The promising candidates for mercury ion detection are nitrogen heterocycles. The widely demonstrated Hg^{2+} chemosensors based on pyrrole, imidazole, pyrazole, pyridine or porphyrin derivatives have proven the possibility to form stable complexes with Hg^{2+} via coordination with N atoms[38–40]. Purine heterocyclic skeleton is characterized by electron delocalization, and there are four nitrogen atoms in the ring providing potential coordination sites for metal ions[21]. Regarding this and above-mentioned reasons, especially biocompatibility and possible cell membrane permeability, we believe that purine-based compounds could be a promising material in terms of optical mercury ion probe development.

In this study, we present a detailed photophysical characterization of 2-piperidinyl-6-triazolylpurine (**PTP**) and its newly synthesized water-soluble derivatives (**PTPa** and **PTPb**). The introduction of electron rich piperidine unit at C2 position of purine core enabled to create a desirable push–pull system while maintaining high fluorescence quantum yields[41,42]. The triazolyl ring was connected to purine core at C6 position via stable C–C bond[43]. This prevented the triazole from acting as a leaving group[44–47] and introduced a metal ion complexing site between nitrogen atoms of the triazole N3 and the purine N7[43,48]. The molecular structure was further extended by electron donating 4-methoxyphenyl at C4 position of triazolyl ring, which allowed for the creation of a donor–acceptor-donor' (D-A-D') type material. **PTP** and its water-soluble derivatives were able to form complexes with several different metal ions. Consequently, the photophysical response and the sensing mechanism were further studied in the presence of metal ions with special attention to Hg^{2+} in aprotic solvents, aqueous media and living cells. Even though purine-based derivatives have already been applied for Cu^{2+} ion recognition in cells[22,49–51], there are only limited examples in the literature of purine-based fluorescent dyes demonstrated as Hg^{2+} chemical probes[52]. Moreover, this is the first time water-soluble purine-based compounds were developed for mercury ion detection and were further applied for intracellular Hg^{2+} imaging.

Results and discussion

Synthesis of PTP and its water-soluble derivatives PTPa and PTPb

The design and synthesis concept of 2-piperidinyl-6-triazolylpurine (**PTP**) was already reported by us recently (Fig. 1a)[43]. We have now developed an approach for the synthesis of modified purine-based chemical sensors **PTPa** and **PTPb** with groups at the N9 position of the purine ring which increase the product solubility in water (Fig. 1b). Firstly, we introduced tetraethylene glycol moiety protected with the THP[53] group at the N9 position via the Mitsunobu reaction. Next, in the Sonogashira reaction, we obtained purine derivative **5**, which was subsequently used in CuAAC with 1-azido-4-methoxybenzene and S_NAr with piperidine, yielding the derivative **6**. The deprotection of the THP group with TFA in methanol (MeOH) gave the first target product, **PTPa**, which was used in photophysical studies and titration experiments and for further modifications. The second target product—a derivative of 3,6,9,12-tetraoxatetradecanoic acid **PTPb** was obtained by alkylation of tetraethylene glycol with *tert*-butyl 2-bromoacetate and further removal of *tert*-butyl protecting group. More details on the synthesis procedures are given in the section Methods and in the Electronic Supplementary Information (ESI), Figs. S1–S14.

Photophysical characterisation of PTP compounds

The photophysical characterization of **PTP** compound was performed in aprotic solvents of different polarities (cyclohexane (CyHex), diethyl ether (Et_2O), ethyl acetate (EtOAc), dimethoxyethane (DME), acetonitrile (MeCN) and dimethyl sulfoxide (DMSO)), while materials **PTPa** and **PTPb** were tested in MeCN and water (see summarized results in Fig. 2 and Table 1).

The absorption band for **PTP** is positioned at ca. 360 nm and remains stable upon increase of solvent's polarity, indicating a weak molecular dipole moment in its ground state (Fig. 2a). The alteration of fluorescence properties is more pronounced, yet not extreme. Fluorescence spectra become structureless and tend to slightly red shift (~ 20 nm). Fluorescence quantum yields (QYs) decrease from 61 to 49% upon changing the solvent from CyHex to MeCN. The fluorescence lifetimes remain relatively long – 9 ns (CyHex) to 12.4 ns (MeCN), indicating quite low cross section for the vertical S_1-S_0 transition. In addition, as it is obvious from fluorescence efficiency values, there is a close competition between radiative and non-radiative excitation decay channels. Furthermore, it is worth noting that the already slow non-radiative decay is even more slowed in viscous DMSO solvent (τ_{nonrad} increase from 24.3 ns in MeCN to 56.1 ns in DMSO), resulting in a significant fluorescence quantum yield increase of up to 72%. This may indicate that photoexcitation in a non-viscous environment is somewhat "lost" through molecular motions.

The newly synthesized water-soluble compounds **PTPa** and **PTPb** possess almost identical excited-state properties to each other in MeCN and water (Fig. 2b). The introduction of aliphatic polyethylene glycol groups helps to increase solubility in water, however, it does not alter the photophysical properties due to the absence of π-conjugation. This is clearly seen from photophysical properties of **PTPa** and **PTPb** in MeCN: the fluorescence quantum yields reach 44%, while fluorescence lifetimes were evaluated to be ca. 11.5 ns, that are very similar to those obtained for **PTP** in the same solvent (QY = 49%; τ = 12.4 ns). While the absorption spectral position remains similar for all compounds, the emission spectra are red shifted by ca. 30 nm for **PTPa** and **PTPb** with respect to **PTP** in MeCN. This red shift can probably result from intramolecular hydrogen bonding enhancement between purine N7 and proton of OH or COOH located at the end of a flexible polyethylene glycol chain in excited state. In water, the fluorescence QY values drop to 17%, while the fluorescence lifetimes are shortened to ca. 7 ns. The quenching of fluorescence in water is expected due to high-energy vibrations of OH groups[54], however, the obtained QY values are considered to be sufficient for further sensing applications in water.

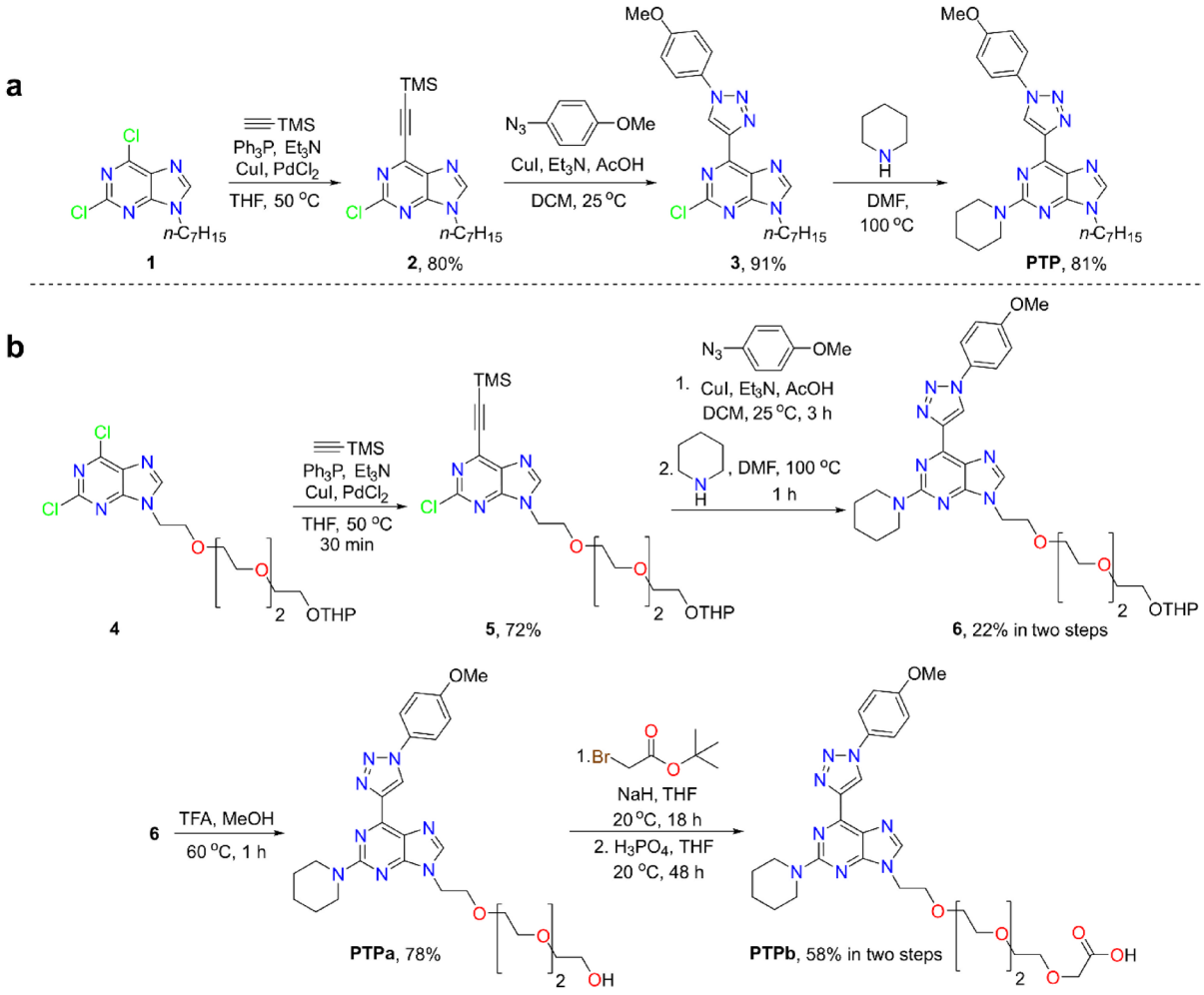

Fig. 1. Synthesis of **PTP** (**a**) and its water-soluble derivatives **PTPa** and **PTPb** (**b**).

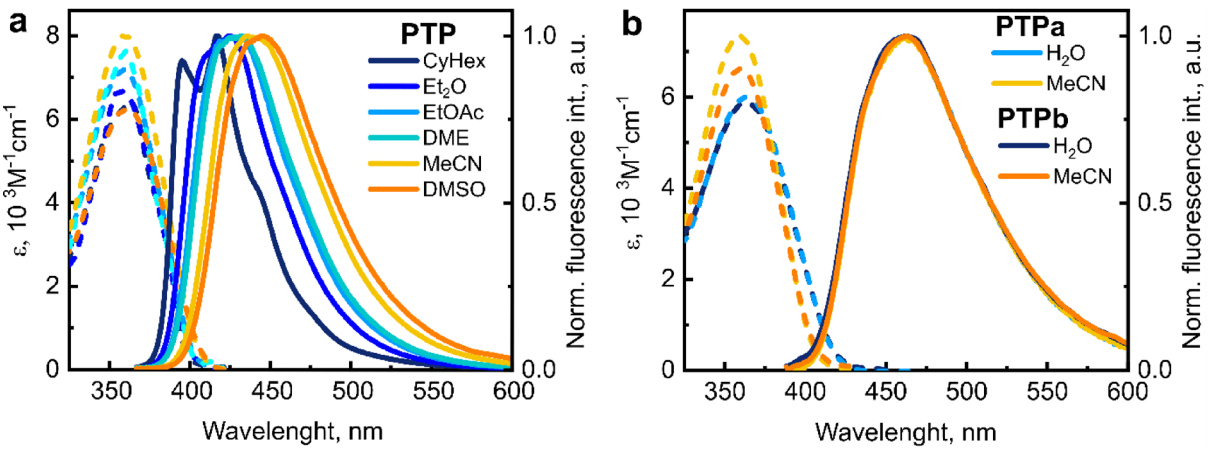

Fig. 2. The absorption (dotted lines) and fluorescence (solid lines) spectra of **PTP** in different solvents, indicated in the legend (**a**). **PTPa** and **PTPb** in MeCN and water (**b**).

Compound	Solvent	ε^1, l/(mol*cm)	$\lambda_{ab}{}^2$, nm	$\lambda_{fl}{}^3$, nm	QY[4], %	τ^5, ns	$\tau_{rad}{}^6$, ns	$\tau_{nonrad}{}^7$, ns
PTP	CyHex	6447	365	415 395	61	9	14.8	23.1
	Et_2O	6715	360	425	52	9.4	18.1	19.6
	EtOAc	7162	360	425	48	9.3	19.4	17.9
	DME	7639	360	425	50	9.7	19.4	19.4
	MeCN	8026	360	435	49	12.4	25.3	24.3
	DMSO	6268	360	445	72	15.7	21.8	56.1
PTPa	MeCN	7342	360	460	44	11.6	26.4	20.7
	H_2O	6005	363	462	17	7.1	41.5	8.5
PTPb	MeCN	6604	360	460	44	11.5	26.2	20.5
	H_2O	5273	363	462	17	7.1	41.8	8.6

Table 1. Steady-state absorption, fluorescence and time-resolved fluorescence spectroscopic data of compound **PTP** in different solvents and compounds **PTPa** and **PTPb** in MeCN and water. [1]Molar extinction coefficients at wavelengths of absorption maxima. [2]Wavelengths of absorption spectra maxima. [3]Wavelengths of fluorescence spectra maxima, obtained by excitation at absorption maxima. [4]Fluorescence quantum yields, determined by the comparative method using quinine sulfate as an etalon. [5]Fluorescence lifetimes. [6]Radiative fluorescence decay lifetimes, $\tau_{rad} = \frac{\tau}{QY}$. [7]Non-radiative fluorescence decay lifetimes, $\tau_{nonrad} = \frac{\tau}{1-QY}$.

To gain insights into potential application of the presented molecules as chemical metal ion sensors, titration experiments with metal ion salts in MeCN and water and the discussion on the sensing mechanism will be presented in the upcoming sections.

Metal ion recognition by PTP in acetonitrile

Steady-state absorption and fluorescence titration experiments were performed using alkali (Na^+ and K^+), alkaline earth (Mg^{2+}, Ca^{2+}), transition (Fe^{2+}, Cu^{2+}, Zn^{2+}, Hg^{2+}) and other (Pb^{2+}) metal ions. The C–C-linked triazole to the purine core enabled triazole complexation with metal ions at its N3 and purine complexation at its N7 (see ^{1}H-NMR titration experiments with metal salts, Figs. S15–S21 in the ESI).

Upon the addition of mercury salts into the **PTP** – MeCN solution, the gradual absorption spectrum red shift and the formation of a new absorption band peaking at 382 nm are observed. The complexation of metal ions with triazole N3 and purine N7 enhances their electron acceptor properties, thus the absorption energy is decreased until the ligand–metal complex is completely formed with its own characteristic absorption band. The changes in fluorescence spectra in the presence of metal ions are dramatic: the fluorescence spectra are gradually quenched until an almost non-emissive state with a spectrum of low intensity peaking at 494 nm is observed (Fig. 3a and Fig. 3a inset).

The absorption and fluorescence spectra amplitude's dependence on mercury ion equivalents (Fig. 3b and c, respectively) indicates identical complexation trends: coordination occurs between two ligands (L) and one metal (M) ion (2L:1 M) (Fig. 3d). The precise complexation pattern was further supported by ^{1}H NMR titration experiments of **PTP** in MeCN-d_3, using benzene as a standard and $Hg(ClO_4)_2{\cdot}3H_2O$ as a Hg^{2+} source and observing the shifts of CH(5) position of triazole and CH(8) position of purine. ^{1}H-NMR spectrum was taken after each addition of the solution containing 0.1 eq. of Hg^{2+} ions to the **PTP** solution in MeCN-d_3. The traces of **PTP** were seen after the addition of 0.5 eq. of Hg^{2+} ions and it fully disappeared after the addition of 0.6 eq. of Hg^{2+} ions (Figs. S15–S16). Furthermore, the HMRS analysis of **PTP** and Hg^{2+} coordination in MeCN showed the same results (Table S14, Figs. S28–S30 in the ESI). Indeed, as already shown by us earlier, the triazolyl-purine compounds can be considered as a general choice for coordination with metal ions[48].

As evident from additional fluorescence and absorption titration experiments (Figs. S31–S32 in the ESI), the **PTP** compound showed a similar response to other transition metal ions, including Fe^{2+}, Cu^{2+}, Zn^{2+} as well as Pb^{2+}: the absorption spectra upon complexation tend to red shift resulting in new absorption bands, while fluorescence intensity is quenched (Fig. 3e and f). A more appealing complexation case is observed for Zn^{2+} that deserves a separate explanation. Both the absorption and fluorescence titration experiments revealed a dual complexation mode of **PTP** that depends on the concentration of zinc ions in the system. Initially, when the concentration of Zn^{2+} ions is 0.5 equivalents and above with respect to the ligand, a complex with general formula [$\mathbf{PTP}_2{\cdot}Zn^{2+}$] is formed. Next, as the zinc ion concentration increases (up to 1 equivalent of Zn^{2+} and above), the initial coordination compound equilibrates with the complex [**PTP**·Zn^{2+}] (see Figs. S17–S21, Table S7 and Figs. S33–S34 in the ESI). As it is seen from the fluorescence titration experiments, the fluorescence of single **PTP** molecules is quenched, nevertheless, the new red shifted fluorescence band arises, with intensity peak value at 480 nm. Thus, the complex [**PTP**·Zn^{2+}] is fluorescent, contrary to what was observed for other metal ions.

Even though the coordination behavior with Zn^{2+} appeared to be interesting and well distinguishable from other metal ions, the titration experiments with water-soluble **PTPa** and **PTPb** compounds showed no evidence of coordination with zinc ions in water (vide infra). Thus, we continue to attain deeper understanding into the complexation mechanism with mercury ions by performing transient absorption measurements and quantum chemical modeling.

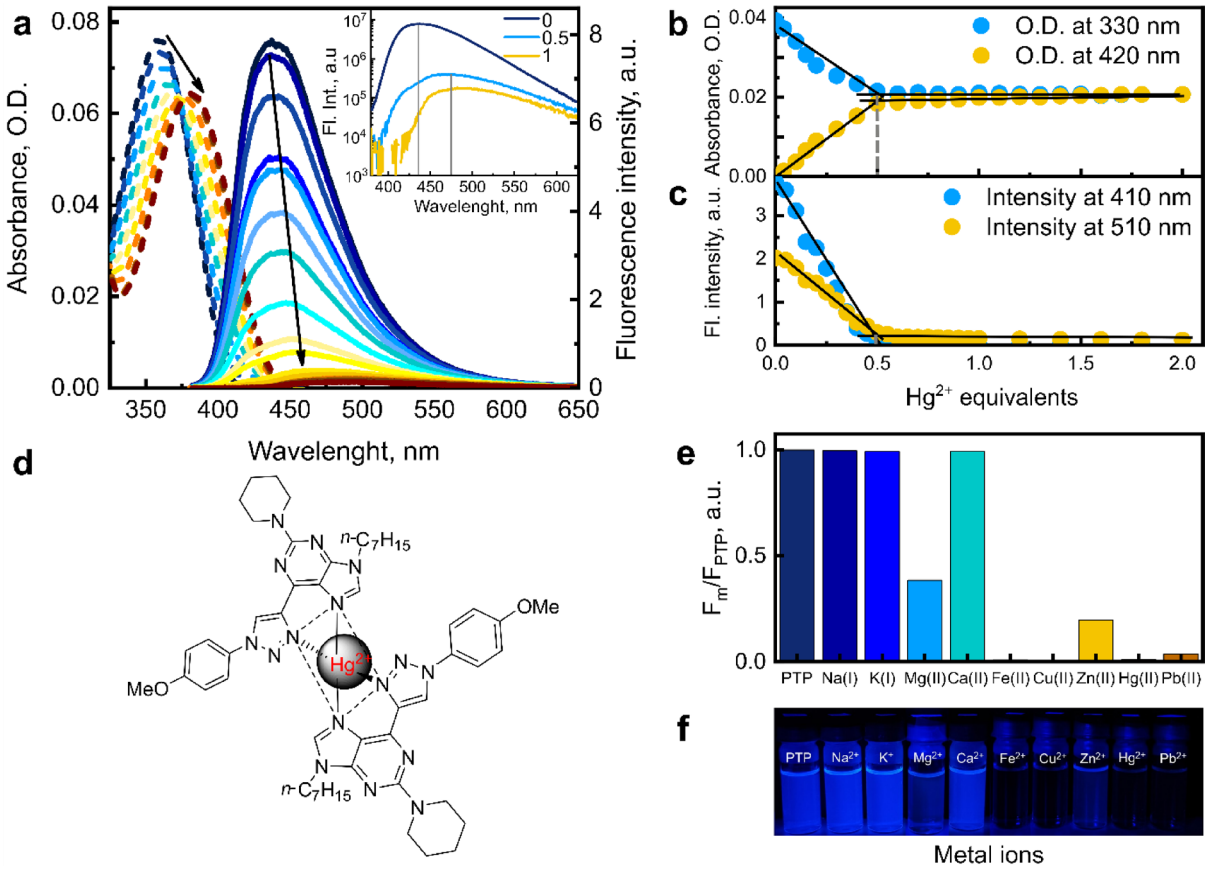

Fig. 3. The absorption and fluorescence spectra response of compound **PTP** to added Hg^{2+} ions in MeCN (**a**). The black curves represent **PTP** absorption (dotted) and fluorescence spectra (solid) with 0 equivalents of Hg^{2+}; the initial titration step for absorption spectra is 0.1 eq., for fluorescence spectra is 0.05 eq. Final titration curves are obtained for **PTP** and 2 equivalents of Hg^{2+} in MeCN. The inset in (**a**) represents fluorescence spectra with 0 eq., 0.5 eq. and 1 eq. of Hg^{2+} in a logarithmic scale. The absorbance (**b**) and fluorescence intensity (**c**) dependence on Hg^{2+} equivalents. Possible complexation mode of 2 **PTP** ligands and 1 mercury ion (**d**). The diagram (**e**) and photograph (**f**) of fluorescence intensity response to 0.5 equivalents of different metal ions.

Femtosecond transient absorption studies

The femtosecond transient absorption (TA) measurements were performed for **PTP** and **PTP** with 0.5 equivalent of Hg^{2+} in MeCN. The excited state absorption (ESA) spectra at 3 ps delay after excitation are shown in Fig. 4 (the spectrum-time resolved maps of ESA and TA signal decay are presented in Figs. S35–S36, ESI). The ESA spectra show narrow and intense absorption bands in the region of 400–430 nm and broad, non-structured absorption bands in the range of 500–850 nm for both samples. Though the ESA spectra are similar for both samples, one will notice that the narrow absorption band at 400–430 nm is red shifted for **PTP**:0.5 Hg^{2+} with respect to the spectral position of the corresponding absorption band of **PTP** by ca. 16 nm.

We assign the "blue" absorption band at 400–430 nm to the transition of the remaining electron in HOMO towards a vacant site in the singly occupied LUMO. This absorption should be somewhat similar to that of a cation radical of the compound or complex. The absorption band in the visible spectral region is the electronic transition from singly occupied LUMO towards higher electronic states. The latter absorption should be similar to that of anion radical of compound or complex. The stimulated emission is not explicitly seen at fluorescence wavelengths, yet the valley in **PTP** spectrum centered at 460 nm may indicate the influence of stimulated emission on the overall spectrum shape. Moreover, the displacement of previously mentioned valley to the red during the first 0.5 ps for **PTP** (see Fig. S35 in the ESI) confirms this suggestion since this is a typical behaviour of dynamic solvation observed for stimulated emission of excited molecular compounds in MeCN.

HOMO – HOMO-1 switching, revealed by quantum chemistry modelling

To gain further insights into the photophysical properties of **PTP** molecule, density functional theory (DFT) and time-dependent (TD) – DFT calculations were performed at the B3LYP/6-31G(d) level employing polarized continuum model (PCM). According to the electron distribution in the highest occupied molecular orbital (HOMO) and the lowest unoccupied molecular orbital (LUMO) in the optimized ground state geometry (Fig. 5a and Fig. S41 in the ESI), both piperidine and purine moieties serve as electron donors, while upon photoexcitation

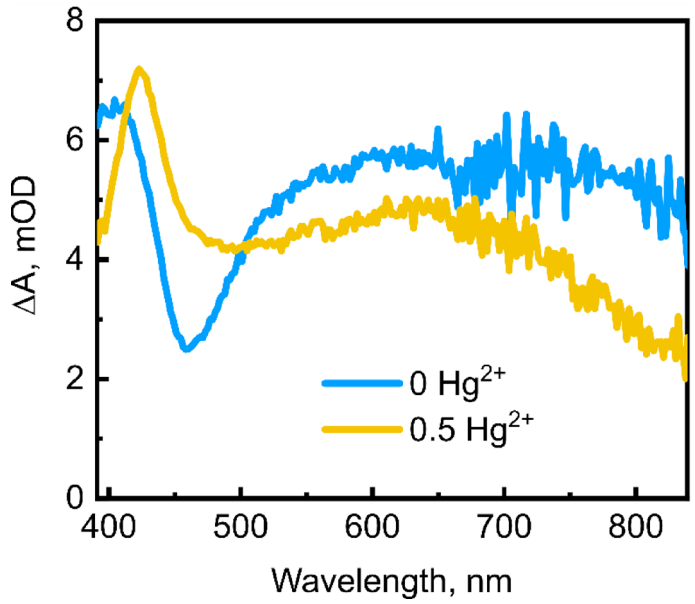

Fig. 4. TA spectra for **PTP** (blue) and **PTP** with 0.5 eq. of Hg^{2+} (yellow) observed at 3 ps delay after excitation.

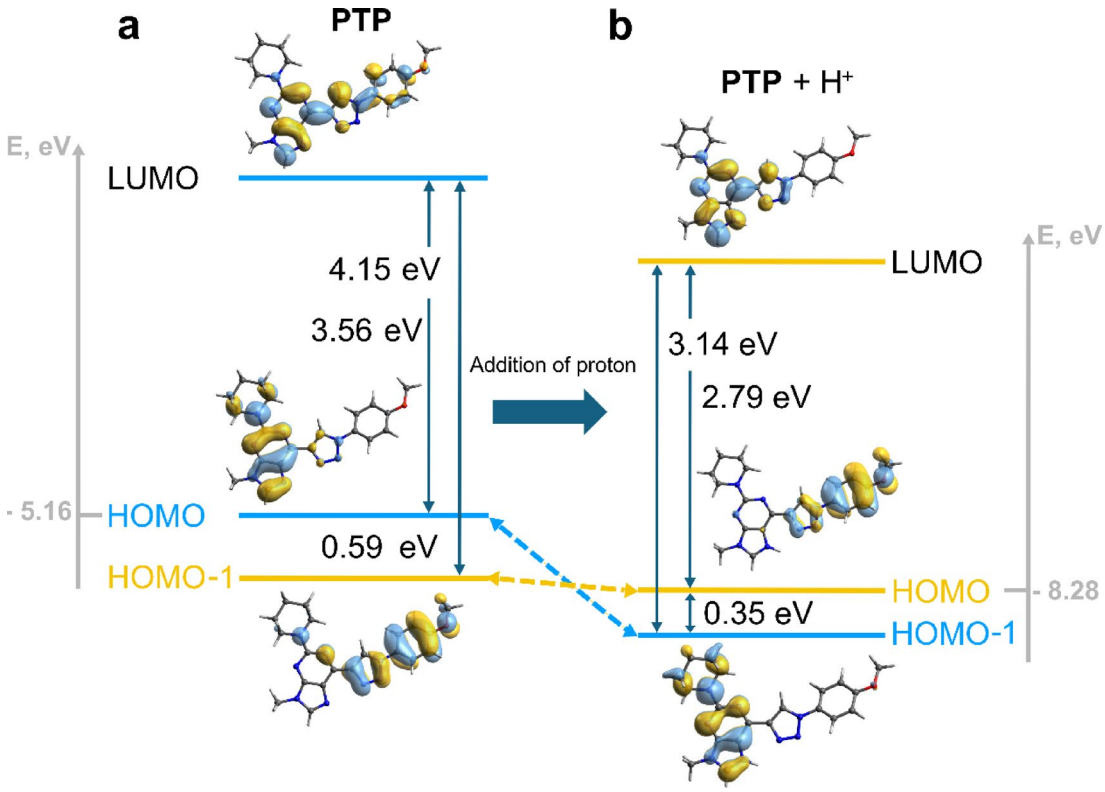

Fig. 5. The HOMO-1, HOMO and LUMO orbital distribution and energy diagrams of **PTP** compound (**a**) and of **PTP** with added proton (**PTP** + H^+) (**b**), calculated with optimized ground state geometry in vacuum. Calculated ionization potentials are -5.15 eV for **PTP** and -8.28 eV for **PTP** + H^+.

charge is redistributed towards the purine-triazole fragment and slightly on the 4-methoxyphenyl fragments. Optimized S_1 geometry and polar acetonitrile environment determined only negligible HOMO–LUMO charge distribution changes in comparison to optimized S_0 geometry in vacuum (Fig. S41, ESI). The calculated electronic absorption spectrum involves only HOMO–LUMO transition and the estimated transition energy of 3.56 eV (Table S15, ESI) corresponds well to the maximum of the lowest energy steady state absorption band

at 360–365 nm. The next optically active electronic transition occurs at 4.74 eV (290 nm) and corresponds to HOMO-1–LUMO transition.

In order to estimate the photophysical properties of the complexed compound, while maintaining the simplicity of the modelled system, the geometry of the protonated compound (**PTP** + H^+) was optimized in its ground state. Interestingly, the localization of HOMO and HOMO-1 molecular orbitals are inversed in the complex as compared with the neutral compound. The HOMO is now located on methoxyphenyl-triazole and HOMO-1 on the purine-piperidine fragment (Fig. 5b). This inversion may be easily understood since the positive proton charge cancels the excess negative charge of piperidine nitrogen due to H^+ incorporation into the aromatic electronic system of purine, while the remaining part of the compound is much less affected. The optical excitation creates a charge transfer state with negative charge shift from methoxyphenyl towards protonated purine.

The exchange of HOMO and HOMO-1 electronic levels upon complexation with cations can also explain the observed differences in TA spectra for **PTP** and **PTP** with 0.5 eq. of Hg^{2+} shown in Fig. 4. Indeed, the electron donating and the electron accepting parts in two samples are different, so the optical absorption of cationic fragments changes from 400 nm for piperidine-purine to 415 nm for methoxybenzene, which is the usual absorption wavelength already observed for this donor (as an example, see Fig. 5a in reference[55]). Similarly, the absorption of the anionic fragment is also different, showing spectral shifts and intensity changes.

The absence of fluorescence in **PTP** with mercury ions also suggests that after excitation at 360 nm, we observe an entire electron charge shift from methoxybenzene to the purine-triazole complex with mercury ion in the sub-picosecond time range leading to a formation of a radical pair. Yet, the relaxation of optical transient absorption spectral bands with a time constant of 1.7 ns shows a quite long charge recombination time (Fig. S36, ESI).

Metal ion recognition by PTPa and PTPb in water

The promising metal ion coordination results of **PTP** in organic aprotic solvents and its fluorescent water-soluble derivatives encouraged us to extend this study by performing titration experiments in water. As presented in Fig. 6a and b, both molecules **PTPa** and **PTPb** form complexes with mercury ions in water. The coordination determines the red shift of the absorption spectra and results in new absorption bands peaking at 377 nm (**PTPa**) and 381 nm (**PTPb**). The fluorescence spectra are obviously quenched, though, not completely and without spectral shifts. These experiments highly resemble those obtained for **PTP** in MeCN in the presence of Hg^{2+}. However, the complexation occurs at a ligand : Hg^{2+} ratio 1 : 1 for both molecules as seen from Fig. 6c and d, which is a consequence of a reduced binding constant in water.

The titration experiments with **PTPa** and **PTPb** in water with other metal ions (Fe^{2+}, Cu^{2+}, Zn^{2+} and Pb^{2+}) revealed that besides mercury ions, molecules coordinate only with Cu^{2+} (Figs. 6e and S37–S40). In general, it is well known that coordination of molecular probes with metal ions is less likely to occur in water than in an aprotic environment. This is mainly determined by solvation effects: water molecules may form hydration shells around metal ions and molecular probes, impeding the approach to each other. However, it is known that Cu^{2+} ion as a Lewis acid is more azaphilic than oxophilic[56,57], therefore it still prefers to complex with nitrogen ligands in aqueous solutions. Mercury salts, even if they are easy to hydrolyze, do not possess any noticeable oxophilicity and thus also can be complexed by nitrogen ligands[58] in the presence of water. On the other hand, Zn^{2+} and Fe^{2+} are rather oxophilic and therefore in aqueous medium as solvent outperforms nitrogen-based ligands[58]. Nevertheless, in the present case, the interference of water molecules in forming complexes with metal ions for studied **PTPa** and **PTPb** derivatives may turn out to be a major advantage, as selectivity towards mercury ions increases.

Imaging of mercury ions in living cells by PTPa

The reasonably good sensitivity of our studied **PTPa** and **PTPb** derivatives towards mercury ions in water and the low toxicity of some **PTP** derivatives studied in our previous work[43], encourage further experiments on presented materials in living cells. Both **PTPa** and **PTPb** were used to treat living cells. However, the **PTPb** material with a COOH moiety in its aliphatic chain appeared to be too reactive as it strongly adheres to the cultural plate. Thus, we continued the experiments with **PTPa** derivative.

To evaluate the capability of **PTPa** for Hg^{2+} imaging in living cells, MDA MB 231 cells were incubated in the presence and absence of $HgCl_2$ (10 μM) for 30 min to facilitate cellular uptake of Hg^{2+} ions. After this preincubation, the cells were treated with **PTPa** (50 μg/mL) for 30 min. Bright field and fluorescence microscopy was employed to assess the behaviour of **PTPa** within the cells (Fig. 7). The images clearly demonstrate that **PTPa** can be efficiently internalized by the cells, as indicated by its fluorescent signal. Furthermore, the material exhibits a fluorescence quenching effect in the mercury enriched environment, which suggests that the quenching of **PTPa** is directly correlated with the intracellular mercury concentration. This observation confirms the material's potential sensitivity to Hg^{2+} ions and its viability for imaging in biological systems where mercury's concentration plays a critical role.

Conclusions

The photophysical behaviour as well as spectroscopic titration response to different metal ions were studied for 2-piperidinyl-6-triazolylpurine **PTP** compound and further expanded to newly synthesized water soluble **PTPa** and **PTPb** derivatives. The piperidine unit at the C2 position of the purine core and 4-methoxyphenyl at the C4 position of the triazolyl ring allowed for the creation of charge transfer type molecules with a D-A-D' structure. The water soluble **PTPa** and **PTPb** demonstrated similar behaviour to **PTP** in MeCN, with fluorescence quantum yield of 49% for **PTP** and 44% for its derivatives. In water, the fluorescence quantum yields remained relatively high – 17% for **PTPa** and **PTPb**. The triazolyl ring, connected to the purine core at the C6 position

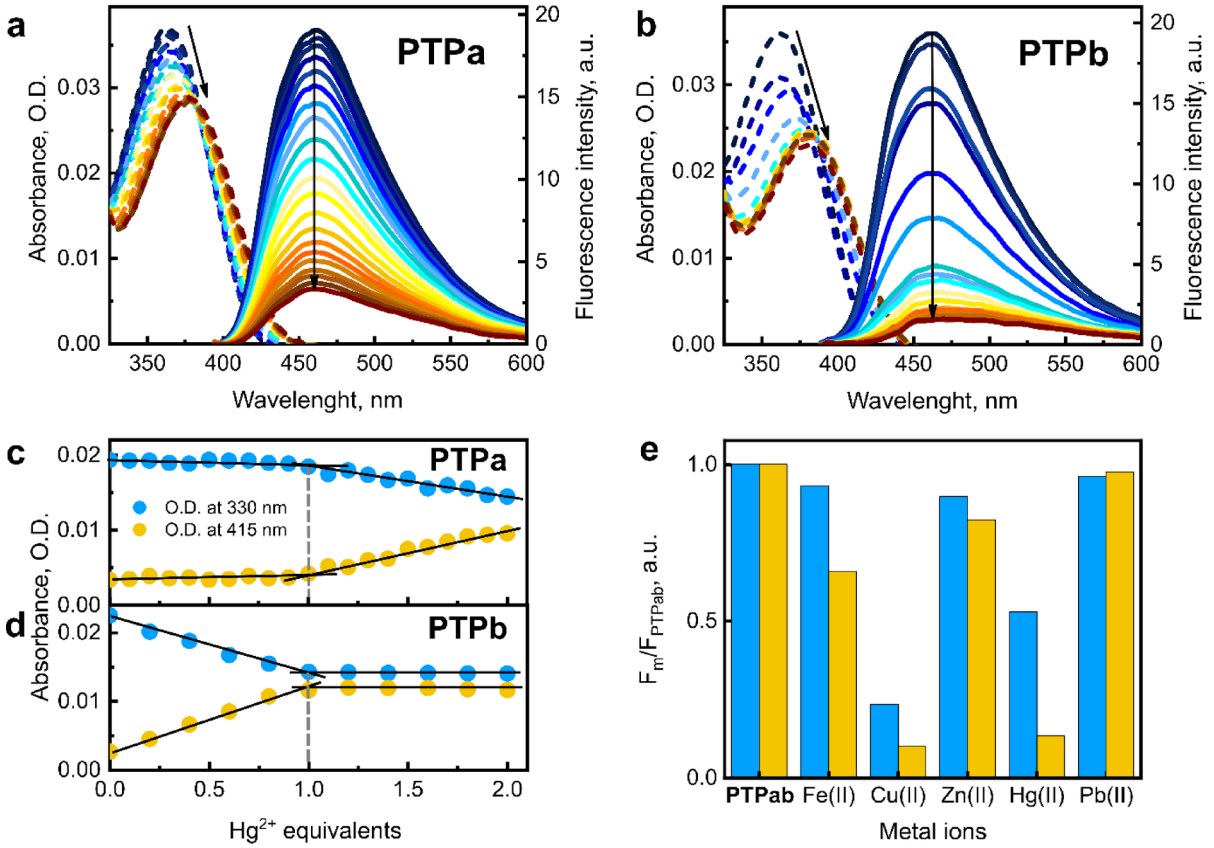

Fig. 6. Absorption and fluorescence spectra response of compounds **PTPa** (**a**) and **PTPb** (**b**) upon addition of Hg^{2+} ions in water. The absorbance intensity dependence on Hg^{2+} equivalents at different wavelengths for **PTPa** (**c**) and **PTPb** (**d**). The fluorescence spectra intensity response to the added 1 equivalent of different metal ions of **PTPa** (blue columns) and **PTPb** (yellow columns) (**e**).

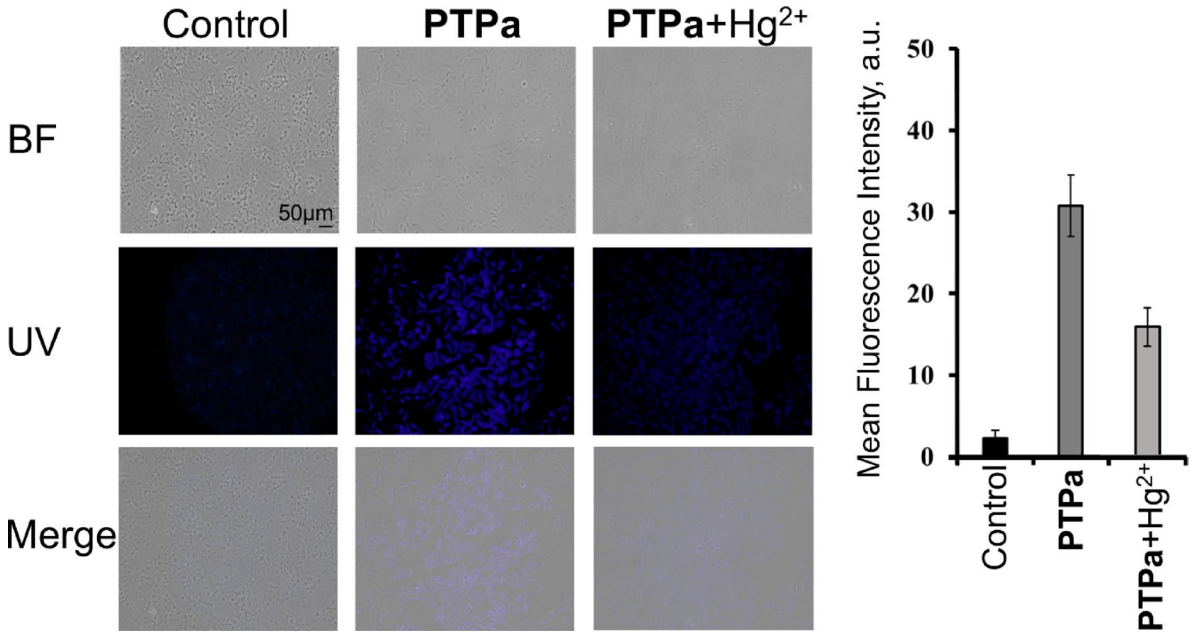

Fig. 7. Bright-field and fluorescence microscopy images of MDA-MB-231 cells stained with **PTPa** (50 μg/mL) and treated with $HgCl_2$ (10 μM). The top row displays bright-field images showing the general cell morphology, while the middle and bottom rows depict fluorescence images illustrating **PTPa** fluorescence and its quenching in the presence of mercury ions.

via stable C–C bond, allowed to introduce a metal ion complexing site between nitrogen atoms of the triazole N3 and the purine N7. Indeed, the studied molecules tend to form complexes with metal ions, including Hg^{2+}. The coordination with mercury ions determines the switching between donors and thus, electronically different HOMO–LUMO transitions occur. The absorption and fluorescence titration experiments of **PTPa** and **PTPb** in water revealed an improved selectivity towards Hg^{2+}. The favourable properties of water-soluble compounds encouraged the successful demonstration of **PTPa** as a Hg^{2+} "turn-off" fluorescence probe in living cells.

Methods

Synthesis: general information

Commercially available reagents were used without further purification. The reactions were monitored by HPLC and TLC analysis. Silica gel 60 F254 aluminum plates (Merck) were used for TLC, achieving visualization with UV light. Column chromatography was carried out on 60 Å, 40–63 μm silica gel. Infrared spectra were recorded using a Thermo Scientific Nicolet™ iSTM50 spectrometer in the Attenuated Total Reflectance (ATR) mode over the range from 400 to 4000 cm-1 (co-adding 64 scans at 4 cm^{-1} resolution and deducting background spectrum from the sample spectrum before every measurement). ^{1}H and ^{13}C NMR spectra were recorded with a Bruker Avance 500 spectrometer in chloroform-d ($CDCl_3$) or acetonitrile-d_3 (MeCN-d_3) at 500 MHz for ^{1}H NMR spectra and 126 MHz for ^{13}C NMR spectra. Chemical shifts (δ) are reported in ppm and coupling constants (*J*) in Hz. The proton ($CDCl_3$ δ = 7.26 ppm; MeCN-d_3 δ = 1.94 ppm) and carbon signals ($CDCl_3$ δ = 77.16 ppm) for residual non-deuterated solvents were used as an internal reference for ^{1}H and ^{13}C NMR spectra, respectively. The multiplicity is assigned using standard abbreviations. The Agilent Technologies 1200 Series system was used to perform HPLC analyses, using an XBridge C_{18} column (4.6 × 150 mm, particle size 3.5 μm). Eluent A (0.1% TFA, 5% MeCN in H_2O) and eluent B (100% MeCN) were used as the mobile phase with a flow rate of 1 mL/min, using following gradient (30 to 95% of eluent B at 0–5 min; 95% of eluent B at 5–10 min; from 95 to 30% of eluent B at 10–12 min). Wavelength of detection – 260 nm. High-resolution mass spectra (ESI) were recorded with a Thermo Fisher Scientific Orbitrap Exploris 120 mass spectrometer operating in the Full Scan mode at the 120,000 resolutions. Similar procedure for synthesis and characterization was already described by us elsewhere[43,48].

Synthesis and characterization of products

2,6-Dichloro-9-(2-(2-(2-(2-((tetrahydro-2H-pyran-2-yl)oxy)ethoxy)ethoxy)ethoxy)ethyl)-9H-purine (4)

A solution of 2,6-dichloropurine (1.0 g, 5.29 mmol, 1.0 equiv.), 2-(2-(2-((tetrahydro-2*H*-pyran-2-yl)oxy) ethoxy)ethoxy)ethan-1-ol[53] (2.22 g, 7.98 mmol, 1.5 equiv.) and triphenylphosphine (Ph_3P) (1.46 g, 5.57 mmol, 1.1 equiv.) in anhydrous tetrahydrofuran (THF) (20 mL) was cooled to 0 °C. DIAD (1.10 mL, 5.60 mmol, 1.1 equiv.) was added dropwise, the mixture was stirred for 2 h at 20 °C. The reaction's completion was assessed using HPLC and then evaporated to dryness. The crude product was purified by flash column chromatography (ethyl acetate (EtOAc)/methanol (MeOH), 0% → 5%). Yield 1.6 g, 69%. Yellowish oil. IR, ν (cm^{-1}): 2983, 2866, 1594, 1553, 1438, 1347, 1304, 1232, 1202, 1143, 1118, 1074, 1032, 986. ^{1}H-NMR (500 MHz, $CDCl_3$) δ (ppm): 8.36 (s, 1H, H-C(8)), 4.61 (t, 1H, ^{3}J = 3.5 Hz, (-CH-)), 4.44 (t, 2H, ^{3}J = 4.8 Hz, ($-CH_2-$)), 3.89–3.81 (m, 4H, 2 × ($-CH_2-$)), 3.69–3.57 (m, 11H, 5 × ($-CH_2-$), H_a-CH), 3.51–3.46 (m, 1H, H_b-CH), 1.85–1.46 (m, 6H, 3 × ($-CH_2-$)). ^{13}C-NMR (75.5 MHz, $CDCl_3$) δ (ppm): 153.3, 152.8, 151.7, 147.6, 130.8, 99.2, 70.79, 70.77, 70.74, 70.72, 70.65, 68.9, 66.8, 62.5, 44.4, 30.7, 25.6, 19.7. HRMS (ESI+): calculated [$C_{18}H_{26}Cl_2N_4O_5 + H^+$] 449.1353 found 449.1341 (2.67 ppm).

2-Chloro-9-(2-(2-(2-(2-((tetrahydro-2H-pyran-2-yl)oxy)ethoxy)ethoxy)ethoxy)ethyl)-6-((trimethylsilyl)ethynyl)-9H-purine (5)

To a solution of compound **4** (800 mg, 1.78 mmol, 1.0 equiv.), Ph_3P (93 mg, 0.04 mmol, 0.2 equiv.), CuI (34 mg, 0.39 mmol, 0.1 equiv.), $PdCl_2$ (32 mg, 0.02 mmol, 0.1 equiv.) in dry THF (25 mL), triethylamine (Et_3N) (1.23 mL, ρ = 0.73 g/cm^3, 8.9 mmol, 5.0 equiv.) was added and the reaction mixture was stirred at 20 °C for 5 min. Then, trimethylsilylacetylene (1.01 mL, ρ = 0.69 g /cm^3, 7.1 mmol, 4.0 equiv.) was added, and the reaction mixture was stirred for 30 min at 50 °C. After reaction completion (monitored by HPLC), the reaction mixture was evaporated, and dried in a vacuum, and the product was purified by flash column chromatography (dichloromethane (DCM)/MeCN, gradient 0% → 10%). Yield: 659 mg, 72%. Yellowish oil. IR, ν (cm^{-1}): 2927, 2919, 2854, 1570, 1497, 1453, 1381, 1345, 1313, 1250, 1207, 1121, 1074, 1032, 1019, 987. ^{1}H-NMR (500 MHz, $CDCl_3$) δ (ppm): 8.30 (s, 1H, H-C(8)), 4.56 (t, 1H, ^{3}J = 3.5 Hz, (-CH-)), 4.39 (t, 2H, ^{3}J = 4.8 Hz, ($-CH_2-$)), 3.83–3.75 (m, 4H, 2 × ($-CH_2-$)), 3.63–3.53 (m, 11H, 5 × ($-CH_2-$), H_a-CH), 3.46–3.41 (m, 1H, H_b-CH), 1.81–1.47 (m, 6H, 3 × ($-CH_2-$)), 0.28 (s, 9H, 3 × ($-CH_3$)). ^{13}C-NMR (75.5 MHz, $CDCl_3$) δ (ppm): 153.7, 153.5, 147.7, 142.2, 133.5, 107.4, 99.0, 97.6, 70.7, 70.61, 70.59, 70.5, 68.8, 66.7, 62.3, 43.9, 30.6, 25.4, 19.6, -0.4. HRMS (ESI+): calculated [$C_{23}H_{35}ClN_4O_5Si + H^+$] 511.2138 found 511.2127 (2.15 ppm).

2-Chloro-6-(1-(4-methoxyphenyl)-1H-1,2,3-triazol-4-yl)-9-(2-(2-(2-(2-((tetrahydro-2H-pyran-2-yl)oxy)ethoxy) ethoxy)ethoxy)ethyl)-9H-purine (5)*

To a solution of compound **5** (600 mg, 1.17 mmol, 1.0 equiv.) in DCM (10 mL) CuI (33 mg, 0.02 mmol, 15 mol%), Et_3N (180 μL, ρ = 0.73 g/mL, 1.29 mmol, 1.1 equiv.), acetic acid (AcOH) (75 μL, ρ = 1.05 g/mL, 1.29 mmol, 2.2 equiv.) and 1-azido-4-methoxybenzene solution in DCM (2.20 mL, C = 0.8 M, 1.76 mmol, 1.5 equiv.) were added. The reaction mixture was stirred for 3 h at 25 °C and monitored by HPLC. Then the reaction mixture was diluted with DCM (20 mL), washed with saturated Na-EDTA solution (2 × 5 mL) and saturated NaCl solution, dried over anhydrous Na_2SO_4, filtered, and evaporated under vacuum. The crude product was purified by flash column chromatography. (EtOAc/MeOH, gradient 0% → 7%). Yield 240 mg, 35%. Yellowish solid. IR, ν (cm^{-1}): 3065, 2937, 2861, 1585, 1519, 1454, 1333, 1247, 1156, 1092, 1076, 1030. ^{1}H-NMR (500 MHz,

$CDCl_3$) δ (ppm): 9.07 (s, 1H, H-C(triazole)) 8.37 (s, 1H, H-C(8)), 7.77, 7.06 (2d, 4H, ^3J = 8.8 Hz, Ar), 4.60 (t, 1H, ^3J = 3.5 Hz, (-CH-)), 4.48 (t, 2H, ^3J = 4.8 Hz, (-CH_2-)), 3.89 (s, 3H, (-OCH_3)) 3.88–3.82 (m, 4H, 2 × (-CH_2-)), 3.68–3.59, 3.49–3.45 (2 m, 12H, 6 × (-CH_2-)), 1.84–1.76, 1.72–1.66, 1.60–1.46 (3 m, 6H, 3 × (-CH_2-)). ^{13}C-NMR (75.5 MHz, $CDCl_3$) δ (ppm): 160.3, 154.5, 154.0, 148.8, 147.3, 143.6, 130.2, 128.8, 125.2, 122.6, 115.0, 99.1, 70.8 (2C), 70.72, 70.68, 70.65, 69.1, 66.8, 62.4, 55.8, 43.9, 30.7, 25.5, 19.6. HRMS (ESI+): calculated [$C_{27}H_{34}ClN_7O_6$ + H^+] 588.2332 found 588.2307 (4.25 ppm).

6-(1-(4-Methoxyphenyl)-1H-1,2,3-triazol-4-yl)-2-(piperidin-1-yl)-9-(2-(2-(2-(2-((tetrahydro-2H-pyran-2-yl)oxy) ethoxy)ethoxy)ethoxy)ethyl)-9H-purine (6)

To a solution of compound **5*** (200 mg, 0.34 mmol, 1.0 equiv.) in dimethylformamide (DMF) (10 mL), piperidine (100 µL, ρ = 0.86 g/mL, 1.02 mmol, 3.0 equiv.) was added and the reaction mixture was stirred for 60 min at 100 °C. The reaction mixture was evaporated and dried in a vacuum and purified by flash column chromatography (EtOAc/MeOH, gradient 0% → 8%). Yield: 138 mg, 64%. Brown oil. IR, ν (cm^{-1}): 2930, 2852, 1671, 1606, 1588, 1517, 1444, 1254, 1122, 1075, 1031, 987. ^{1}H-NMR (500 MHz, $CDCl_3$) δ (ppm): 9.01 (s, 1H, H-C(triazole)) 7.93 (s, 1H, H-C(8)), 7.76, 7.04 (2d, 4H, ^3J = 8.8 Hz, Ar), 4.61 (t, 1H, ^3J = 3.5 Hz, (-CH-)), 4.32 (t, 2H, ^3J = 4.8 Hz, (-CH_2-)), 3.96–3.92 (m, 4H, 2 × (-CH_2-)), 3.88 (s, 3H, (-OCH_3)), 3.87–3.82 (m, 4H, 2 × (-CH_2-)), 3.67–3.46 (m, 12H, 6 × (-CH_2-)), 1.83–1.47 (m, 12H, 6 × (-CH_2-)). ^{13}C-NMR (75.5 MHz, $CDCl_3$) δ (ppm): 160.1, 159.5, 154.3, 147.28, 145.1, 142.8, 130.6, 124.6, 123.0, 122.7, 114.9, 99.1, 70.8 (2C), 70.75, 70.73, 70.69, 69.4, 66.8, 62.4, 55.8, 45.6, 43.0, 30.7, 26.1, 25.6, 25.1, 19.7. HRMS (ESI+): calculated [$C_{32}H_{44}O_8N_6$ + H^+] 637.3457 found 637.3434 (3.60 ppm).

2-(2-(2-(2-(6-(1-(4-Methoxyphenyl)-1H-1,2,3-triazol-4-yl)-2-(piperidin-1-yl)-9H-purin-9-yl)ethoxy)ethoxy) ethoxy)ethan-1-ol (PTPa)

To a solution of compound **6** (300 mg, 0.47 mmol, 1.0 equiv.) in MeOH (5 mL), TFA (90 µL, 1.18 mmol, 2.5 equiv.) was added. The reaction mixture was stirred at 60 °C for 1 h, then evaporated and purified by reverse phase flash chromatography (MeOH/H_2O). Yield: 204 mg, 78%. Beige solid. IR, ν (cm^{-1}): 2912, 2857, 1603, 1582, 1518, 1469, 1450, 1405, 1353, 1302, 1251, 1211, 1182, 1130, 1093, 1030, 987. ^{1}H-NMR (500 MHz, $CDCl_3$) δ (ppm): 9.28 (s, 1H, H-C(triazole)), 8.23 (s, 1H, H-C(8)), 7.86, 7.03 (2d, 4H, ^3J = 8.8 Hz, Ar), 4.32 (t, 2H, ^3J = 4.4 Hz, (-CH_2-)), 3.97–3.92 (m, 4H, 2 × (-CH_2-)), 3.87 (s, 3H, (-OCH_3)), 3.83 (t, 2H, ^3J = 4.4 Hz, (-CH_2-)), 3.80 (t, 2H, ^3J = 4.3 Hz, (-CH_2-)), 3.70–3.62 (m, 10H, 5 × (-CH_2-)), 1.69–1.62 (m, 6H, 3 × (-CH_2-)). ^{13}C-NMR (75.5 MHz, $CDCl_3$) δ (ppm): 159.9, 159.5, 154.2, 147.3, 144.4, 143.5, 130.8, 124.9, 122.3, 122.2, 114.9, 73.5, 70.8, 70.7, 70.3, 70.25, 69.3, 61.6, 55.8, 45.6, 42.5, 26.1, 25.1. HRMS (ESI+): calculated [$C_{27}H_{36}O_5N_8$ + H^+] 553.2881 found 553.2862 (3.43 ppm).

tert-Butyl 14-(6-(1-(4-methoxyphenyl)-1H-1,2,3-triazol-4-yl)-2-(piperidin-1-yl)-9H-purin-9-yl)-3,6,9,12-tetraoxatetradecanoate (PTPa)*

To a solution of compound **PTPa** (100 mg, 0.18 mmol, 1.0 equiv.) and NaH (22 mg, 0.54 mmol, 3.0 equiv.) in THF (4 mL) *tert*-butyl 2-bromoacetate (183 µL, 1.44 mmol, 8.0 equiv.) was added. The reaction mixture was stirred at 20 °C for 18 h, and then 10% acetic acid solution (1 mL) was added, and the reaction mixture was evaporated under vacuum. The crude product was purified by flash column chromatography (EtOAc/MeOH, gradient 0% → 5%). Yield: 85 mg, 71%. Yellow oil. IR, ν (cm^{-1}): 2927, 2919, 2854, 1745, 1606, 1588, 1517, 1461, 1445, 1368, 1304, 1254, 1126, 1032, 988. ^{1}H-NMR (500 MHz, $CDCl_3$) δ (ppm): 9.01 (s, 1H, H-C(triazole)), 7.94 (s, 1H, H-C(8)), 7.76 (d, 2H, ^3J = 8.9 Hz, Ar), 7.04 (d, 2H, ^3J = 8.9 Hz, Ar), 4.32 (t, 2H, ^3J = 5.2 Hz, (-CH_2-)), 4.00 (s, 2H, (-CH_2-)), 3.96–3.92 (m, 4H, 2 × (-CH_2-), 3.88 (s, 3H, (-CH_3)), 3.84 (t, 2H, ^3J = 5.2 Hz, (-CH_2-)), 3.71–3.66 (m, 4H, 2 × (-CH_2-)), 3.65–3.60 (m, 8H, 4 × (-CH_2-)), 1.69–1.64 (m, 6H, 3 × (-CH_2-), 1.45 (s, 9H, 3 × (-CH_3)). ^{13}C-NMR (75.5 MHz, $CDCl_3$) δ (ppm): 169.8, 160.1, 159.5, 154.3, 147.2, 145.1, 142.8, 130.6, 124.6, 123.0, 122.6, 114.9, 81.7, 70.80, 70.76, 70.72, 70.70, 70.68, 70.66, 69.4, 69.1, 55.8, 45.6, 43.0, 28.2, 26.0, 25.1. HRMS (ESI+): calculated [$C_{33}H_{46}N_8O_7$ + H^+] 667.3562 found 667.3542 (2.99 ppm).

14-(6-(1-(4-Methoxyphenyl)-1H-1,2,3-triazol-4-yl)-2-(piperidin-1-yl)-9H-purin-9-yl)-3,6,9,12-tetraoxatetradecanoic acid (PTPb)

To a solution of compound **PTPa*** (60 mg, 0.09 mmol, 1.0 equiv.) in THF (0.5 mL), aqueous phosphoric acid (0.5 mL, 85 *wt %*) was added. The reaction mixture was stirred at 20 °C for 48 h and then evaporated under vacuum. The crude product was purified by reverse phase flash column chromatography (H_2O/MeOH, gradient 10% → 95%). Yield: 45 mg, 82%. Light yellow solid. IR, ν (cm^{-1}): 2921, 2853, 1732, 1607, 1591, 1517, 1461, 1445, 1350, 1305, 1254, 1108, 1027, 988. ^{1}H-NMR (500 MHz, $CDCl_3$) δ (ppm): 8.90 (s, 1H, H-C(triazole)) 8.11 (s, 1H, H-C(8)), 7.74 (d, 2H, ^3J = 8.4 Hz, Ar), 7.00 (d, 2H, ^3J = 8.4 Hz, Ar), 4.34 (t, 2H, ^3J = 4.5 Hz, (-CH_2-)), 4.12 (s, 2H, (-CH_2-)), 3.94–3.91 (m, 4H, 4 × (-CH_2-), 3.88 (s, 3H, (-CH_3)), 3.84 (t, 2H, ^3J = 4.5 Hz, (-CH_2-)), 3.74–3.70 (m, 2H, (-CH_2-)), 3.68–3.60 (m, 10H, 5 × (-CH_2-)), 1.70–1.56 (m, 6H, 3 × (-CH_2-). ^{13}C-NMR (75.5 MHz, $CDCl_3$) δ (ppm): 174.2, 160.0, 159.3, 154.2, 147.0, 145.2, 143.6, 130.4, 124.0, 122.4, 122.1, 114.8, 70.6, 70.4 (2C), 70.35 (2C), 70.3, 69.7, 69.1, 55.7, 45.5, 42.9, 25.9, 25.0. HRMS (ESI+): calculated [$C_{29}H_{38}N_8O_7$ + H^+] 611.2936 found 611.2912 (3.92 ppm).

Materials and methods for photophysical characterization

Spectroscopic measurements of **PTP** compound were performed in aprotic solvents of different polarities: cyclohexane (CyHex), diethyl ether (Et_2O), ethyl acetate (EtOAc), dimethoxyethane (DME), acetonitrile (MeCN) and dimethyl sulfoxide (DMSO). All solvents were purchased from Sigma Aldrich and were of spectroscopic or HPLC grade. The following salts for the UV and NMR titration experiments were also purchased from Sigma Aldrich: $NaClO_4$, $KClO_4$, $Mg(ClO_4)_2$, $Ca(ClO_4)_2{\cdot}4H_2O$, $FeCl_2O_8{\cdot}H_2O$, $CuCl_2O_8{\cdot}6H_2O$, $ZnCl_2O_6{\cdot}6H_2O$,

$Hg(ClO_4)_2{\cdot}3H_2O$, $Pb(ClO_4)_2$. Purified grade 2 water (Compact Pure, Adrona) was used for spectroscopic measurements of **PTPa** and **PTPb**.

The concentrations for fluorescence quantum yield measurements were selected so the absorbance at excitation wavelength would be in a range 0.03–0.08. For absorption and fluorescence measurements (including titration experiments) the initial concentration of compounds was 10^{-5} M. Quartz cells of 1 cm were used.

Absorption spectra were measured on a UV–vis–near infrared spectrophotometer Lambda 950 (PerkinElmer); fluorescence spectra were measured using a back-thinned CCD spectrometer PMA-11 (Hamamatsu) and a xenon lamp coupled to a monochromator (full width at half-maximum < 10 meV) as an excitation source. All steady-state fluorescence spectra were obtained by exiting samples to maxima of the lowest-energy absorption bands. Fluorescence quantum yields were determined by comparative method. The concentration of studied compounds in solvents and relative standard quinine sulfate in 0.5 M sulfuric acid (H_2SO_4) were selected so that OD would be around 0.05. Time-resolved fluorescence experiments were conducted by using time-correlated single photon counting system (PicoQuant PicoHarp 300). Femtosecond transient absorption measurements were carried out using commercial spectrometer (Harpia, Light Conversion) pumped with wavelength-tunable optical parametric amplifier (Orpheus, Light Conversion) coupled to 190 fs, 10 kHz pulsed laser (Pharos-SP, Light Conversion). Probe source was white light continuum (WLC) pulses generated by focusing the fundamental 1030 nm harmonic in purified water flowing inside quartz cuvette coupled to home-built flow system. The angle between linearly polarized pump and probe pulses was set to approximately 54 degrees. Samples were excited at 360 nm. The employed photophysical measurements' methods and setups are similar to those already described by us elsewhere[48].

NMR titration experiments with metal salts

NMR titration was done in MeCN-d_3, using benzene as a standard and $Hg(ClO_4)_2{\cdot}3H_2O$ as a Hg^{2+} source or $Zn(ClO_4)_2{\cdot}6H_2O$ as a Zn^{2+} source. In the NMR tube, compound (**PTP**, **PTPa**, or **PTPb**) was dissolved in MeCN-d_3 (0.5 mL), and benzene (1.2 µL) was added to it as an internal standard. The amount of substance was calculated (Tables S1, S4, S8, S11, see Electronic Supplementary Information (ESI)). A solution of $Hg(ClO_4)_2{\cdot}6H_2O$ or $Zn(ClO_4)_2{\cdot}6H_2O$ in MeCN-d_3 with known concentration was prepared (Table S2, S5, S9, S12 in the ESI). Then ^{1}H-NMR spectra were taken (for 0 eq.). After that, the calculated amount of the titrant (0.10, 0.20, 0.30 equiv. etc., Tables S3, S6, S10, S13 in the ESI) was added to the NMR tube, which was shaken vigorously before taking the next ^{1}H-NMR spectrum. This procedure was repeated by adding the desired amount of titrant and taking ^{1}H-NMR spectra. All spectra were calibrated using a benzene signal at 7.37 ppm, then stacked, and their signal shift was analyzed. The full set of NMR titration results of **PTP**, **PTPa** and **PTPb** with different metal ions is given in Figs. S15–S27.

DFT modelling

Density functional theory (DFT) calculations for **PTP** molecule were performed at the B3LYP/6-31G(d) level employing polarized continuum model (PCM). Excitation energy calculations and excited state optimization were performed using time-dependent (TD)—DFT with the same basis set. Calculations were performed using Gaussian 09W software[59]. The theoretical evaluation of complexed **PTP** compound was carried out by introducing a proton (H^+) between nitrogen atoms of the triazole N3 and the purine N7 and using the same calculation conditions as previously described.

Data availability

Data associated with this work and presented here (including Supplementary Information) will be made available on request. Correspondence and requests for materials should be addressed to J.J.

Received: 11 March 2025; Accepted: 6 August 2025
Published online: 01 October 2025

References

1. Rosemeyer, H. The chemodiversity of purine as a constituent of natural products. *Chem. Biodivers.* **1**, 361–401. https://doi.org/10.1002/cbdv.200490033 (2004).
2. Parker, W. B. Enzymology of purine and pyrimidine antimetabolites used in the treatment of cancer. *Chem. Rev.* **109**, 2880–2893. https://doi.org/10.1021/cr900028p (2009).
3. Gogineni, V., Schinazi, R. F. & Hamann, M. T. Role of marine natural products in the genesis of antiviral agents. *Chem. Rev.* **115**, 9655–9706. https://doi.org/10.1021/cr4006318 (2015).
4. Seley-Radtke, K. L. & Yates, M. K. The evolution of nucleoside analogue antivirals: A review for chemists and non-chemists. Part 1: Early structural modifications to the nucleoside scaffold. *Antiviral Res.* **154**, 66–86. https://doi.org/10.1016/j.antiviral.2018.04.004 (2018).
5. Hu, Y. et al. Potential antibacterial ethanol-bridged purine azole hybrids as dual-targeting inhibitors of MRSA. *Bioorg. Chem.* **114**, 105096. https://doi.org/10.1016/j.bioorg.2021.105096 (2021).
6. Swennen, E. L. R., Dagnelie, P. C. & Bast, A. ATP inhibits hydroxyl radical formation and the inflammatory response of stimulated whole blood even under circumstances of severe oxidative stress. *Free Radic. Res.* **40**, 53–58. https://doi.org/10.1080/10715760500364298 (2006).
7. Berdis, A. Nucleobase-modified nucleosides and nucleotides: Applications in biochemistry, synthetic biology, and drug discovery. *Front. Chem.* **10**, 1051525. https://doi.org/10.3389/fchem.2022.1051525 (2022).
8. Wong, X. K. & Yeong, K. Y. From nucleic acids to drug discovery: Nucleobases as emerging templates for drug candidates. *Curr. Med. Chem.* **28**, 7076–7121. https://doi.org/10.2174/0929867328666210215113828 (2021).
9. Butler, R. S., Cohn, P., Tenzel, P., Abboud, K. A. & Castellano, R. K. Synthesis, photophysical behavior, and electronic structure of push–pull purines. *J. Am. Chem. Soc.* **131**, 623–633. https://doi.org/10.1021/ja806348z (2009).
10. Matarazzo, A. & Hudson, R. H. E. Fluorescent adenosine analogs: A comprehensive survey. *Tetrahedron* **71**, 1627–1657. https://doi.org/10.1016/j.tet.2014.12.066 (2015).

11. Saito, Y. & Hudson, R. H. E. Base-modified fluorescent purine nucleosides and nucleotides for use in oligonucleotide probes. *J. Photochem. Photobiol. C Photochem. Rev.* **36**, 48–73. https://doi.org/10.1016/j.jphotochemrev.2018.07.001 (2018).
12. Pu, F., Ren, J. & Qu, X. Nucleobases, nucleosides, and nucleotides: Versatile biomolecules for generating functional nanomaterials. *Chem. Soc. Rev.* **47**, 1285–1306. https://doi.org/10.1039/C7CS00673J (2018).
13. Collier, G. S. et al. Linking design and properties of purine-based donor-acceptor chromophores as optoelectronic materials. *J. Mater. Chem. C* **5**, 6891–6898. https://doi.org/10.1039/c7tc01835e (2017).
14. Sebris, A. et al. Homoleptic purine-based NHC iridium (iii) complexes for blue OLED application: Impact of isomerism on photophysical properties. *J. Mater. Chem. C* **11**, 14608–14620. https://doi.org/10.1039/D3TC02681G (2023).
15. Traskovskis, K. et al. All-organic fast intersystem crossing assisted exciplexes exhibiting sub-microsecond thermally activated delayed fluorescence. *J. Mater. Chem. C* **9**, 4532–4543. https://doi.org/10.1039/d0tc05099g (2021).
16. Yang, Y. et al. Ultraviolet-violet electroluminescence from highly fluorescent purines. *J. Mater. Chem. C* **1**, 2867–2874. https://doi.org/10.1039/C3TC00734K (2013).
17. Yang, Y. et al. Blue-violet electroluminescence from a highly fluorescent purine. *Chem. Mater.* **22**, 3580–3582. https://doi.org/10.1021/cm100407n (2010).
18. Wang, H. Y. et al. Three-in-one: Information encryption, anti-counterfeiting and LD-tracking of multifunctional purine derivatives. *J. Mater. Chem. C* **9**, 2864–2872. https://doi.org/10.1039/D0TC05221C (2021).
19. Wang, A. et al. A purine-based fluorescent probe for H2S detection and imaging of cells. *Spectrochim. Acta Part A Mol. Biomol. Spectrosc.* **308**, 123674. https://doi.org/10.1016/j.saa.2023.123674 (2024).
20. Li, J. et al. Nucleoside-based ultrasensitive fluorescent probe for the dual-mode imaging of microviscosity in living cells. *Anal. Chem.* **88**, 5554–5560. https://doi.org/10.1021/acs.analchem.6b01395 (2016).
21. Xu, H.-Y., Chen, W., Zhang, W., Ju, L. & Lu, H. A selective Purine-based fluorescent chemosensor for the "naked-eye" detection of Zinc ion (Zn^{2+}): Applications in live cell imaging and test strips. *New J. Chem.* **44**, 15195–15201. https://doi.org/10.1039/d0nj02687e (2020).
22. Chen, X. et al. Synthesis and application of purine-based fluorescence probe for continuous recognition of Cu^{2+} and glyphosate. *Spectrochim. Acta Part A Mol. Biomol. Spectrosc.* **304**, 123291. https://doi.org/10.1016/j.saa.2023.123291 (2024).
23. Chen, W., Xu, H., Ju, L. & Lu, H. A highly sensitive fluorogenic "turn-on" chemosensor for the recognition of Cd^{2+} based on a hybrid purine-quinoline Schiff base. *Tetrahedron* **88**, 132123. https://doi.org/10.1016/j.tet.2021.132123 (2021).
24. Wu, G. et al. A novel rhodamine B and purine derivative-based fluorescent chemosensor for detection of palladium (II) ion. *Inorg. Chem. Commun.* **102**, 233–239. https://doi.org/10.1016/j.inoche.2019.02.038 (2019).
25. Hong, Y. S., Kim, Y. M. & Lee, K. E. Methylmercury exposure and health effects. *J. Prev. Med. Public Health* **45**, 353–363. https://doi.org/10.3961/JPMPH.2012.45.6.353 (2012).
26. Mercury in Food | FDA. https://www.fda.gov/food/environmental-contaminants-food/mercury-food.
27. Mercury. https://www.who.int/news-room/fact-sheets/detail/mercury-and-health.
28. Health Effects of Exposures to Mercury | US EPA. https://www.epa.gov/mercury/health-effects-exposures-mercury.
29. Wang, Y. et al. Fluorescent probe for mercury ion imaging analysis: Strategies and applications. *Chem. Eng. J.* **406**, 127166. https://doi.org/10.1016/j.cej.2020.127166 (2021).
30. Zhang, Y., Gao, Y., Liu, Q. S., Zhou, Q. & Jiang, G. Chemical contaminants in blood and their implications in chronic diseases. *J. Hazard. Mater.* **466**, 133511. https://doi.org/10.1016/j.jhazmat.2024.13351 (2024).
31. Briffa, J., Sinagra, E. & Blundell, R. Heavy metal pollution in the environment and their toxicological effects on humans. *Heliyon* **6**, e04691. https://doi.org/10.1016/j.heliyon.2020.e04691 (2020).
32. Duan, N. et al. The research progress of organic fluorescent probe applied in food and drinking water detection. *Coord. Chem. Rev.* **427**, 213557. https://doi.org/10.1016/j.ccr.2020.213557 (2021).
33. Saleem, M. & Lee, K. H. Optical sensor: A promising strategy for environmental and biomedical monitoring of ionic species. *RSC Adv.* **5**, 72150–72287. https://doi.org/10.1039/C5RA11388A (2015).
34. Chen, S. Y., Li, Z., Li, K. & Yu, X. Q. Small molecular fluorescent probes for the detection of lead, cadmium and mercury ions. *Coord. Chem. Rev.* **429**, 213691. https://doi.org/10.1016/j.ccr.2020.213691 (2021).
35. Fukuhara, G. Analytical supramolecular chemistry: Colorimetric and fluorimetric chemosensors. *J. Photochem. Photobiol. C Photochem. Rev.* **42**, 100340. https://doi.org/10.1016/j.jphotochemrev.2020.100340 (2020).
36. Yin, J., Hu, Y. & Yoon, J. Fluorescent probes and bioimaging: Alkali metals, alkaline earth metals and pH. *Chem. Soc. Rev.* **44**, 4619–4644. https://doi.org/10.1039/C4CS00275J (2015).
37. Udhayakumari, D., Ramasundaram, S., Jerome, P. & Oh, T. H. A review on small molecule based fluorescence chemosensors for bioimaging applications. *J. Fluoresc.* https://doi.org/10.1007/s10895-024-03826-2 (2024).
38. Tang, A. et al. A multifunctional aggregation-induced emission (AIE)-active fluorescent chemosensor for detection of Zn^{2+} and Hg^{2+}. *Tetrahedron* **75**, 130489. https://doi.org/10.1016/j.tet.2019.130489 (2019).
39. Rios, M. C., Bravo, N. F., Sanchez, C. C. & Portilla, J. Chemosensors based on N-heterocyclic dyes: Advances in sensing highly toxic ions such as CN^- and Hg^{2+}. *RSC Adv.* **11**, 34206–34234. https://doi.org/10.1039/D1RA06567J (2021).
40. Nagarajan, R., Varadaraju, C. & Lee, K. H. Recent advancements in the role of N-Heterocyclic receptors on heavy metal ion sensing. *Dye Pigment* **191**, 109331. https://doi.org/10.1016/j.dyepig.2021.109331 (2021).
41. Sebris, A. et al. Photophysical and electrical properties of highly luminescent 2/6-triazolyl-substituted push-pull purines. *ACS Omega* **7**, 5242–5253. https://doi.org/10.1021/acsomega.1c06359 (2022).
42. Šišuļins, A. et al. Synthesis and fluorescent properties of N(9)-alkylated 2-amino-6-triazolylpurines and 7-deazapurines. *Beilstein J. Org. Chem.* **15**, 474–489. https://doi.org/10.3762/bjoc.15.41 (2019).
43. Burcevs, A. et al. Synthesis of fluorescent C-C bonded triazole-purine conjugates. *J. Fluoresc.* **34**, 1091–1097. https://doi.org/10.1007/s10895-023-03337-6 (2024).
44. Kovaļovs, A. et al. 1,2,3-Triazoles as leaving groups in purine chemistry: A three-step synthesis of N6-substituted-2-triazolyl-adenine nucleosides and photophysical properties thereof. *Tetrahedron Lett.* **54**, 850–853. https://doi.org/10.1016/j.tetlet.2012.11.095 (2013).
45. Novosjolova, I., Bizděna, E. & Turks, M. Application of 2,6-diazidopurine derivatives in the synthesis of thiopurine nucleosides. *Tetrahedron Lett.* **54**, 6557–6561. https://doi.org/10.1016/j.tetlet.2013.09.095 (2013).
46. Krikis, K. E., Novosjolova, I., Mishnev, A. & Turks, M. 1,2,3-Triazoles as leaving groups in SNAr-Arbuzov reactions: Synthesis of C6-phosphonated purine derivatives. *Beilstein J. Org. Chem.* **17**, 193–202. https://doi.org/10.3762/BJOC.17.19 (2021).
47. Cīrule, D., Novosjolova, I., Bizdēna, Ē & Turks, M. 1,2,3-Triazoles as leaving groups: SNAr reactions of 2,6-bistriazolylpurines with O- And C-nucleophiles. *Beilstein J. Org. Chem.* **17**, 410–419. https://doi.org/10.3762/BJOC.17.37 (2021).
48. Jovaisaite, J. et al. Proof of principle of a purine D-A-D′ ligand based ratiometric chemical sensor harnessing complexation induced intermolecular PET. *Phys. Chem. Chem. Phys.* **22**, 26502–26508. https://doi.org/10.1039/d0cp04091f (2020).
49. Tao, X. et al. Sensitive fluorescence detection of glyphosate and glufosinate ammonium pesticides by purine-hydrazone-Cu^{2+} complex. *Spectrochim. Acta Part A Mol. Biomol. Spectrosc.* **314**, 124226. https://doi.org/10.1016/J.SAA.2024.124226 (2024).
50. Shao, Q. et al. Sensing of organophosphorus pesticides by fluorescent complexes based on purine-hydrazone receptor and copper (II) and its application in living-cells imaging. *Spectrochim. Acta Part A Mol. Biomol. Spectrosc.* **296**, 122676. https://doi.org/10.1016/J.SAA.2023.122676 (2023).
51. Amer, S., El-Wakiel, N. & El-Ghamry, H. Synthesis, spectral, antitumor and antimicrobial studies on Cu(II) complexes of purine and triazole Schiff base derivatives. *J. Mol. Struct.* **1049**, 326–335. https://doi.org/10.1016/J.MOLSTRUC.2013.06.059 (2013).

52. Gao, S. H. et al. Highly selective detection of Hg^{2+} ion by push-pull-type purine nucleoside-based fluorescent sensor. *Tetrahedron* **70**, 4929–4933. https://doi.org/10.1016/j.tet.2014.05.050 (2014).
53. Ansell, S. M. Polyamide oligomers (2001).
54. Maillard, J. et al. Universal quenching of common fluorescent probes by water and alcohols. *Chem. Sci.* **12**, 1352–1362. https://doi.org/10.1039/D0SC05431C (2021).
55. Panchenko, P. A., Fedorov, Y. V., Fedorova, O. A. & Jonusauskas, G. FRET versus PET: Ratiometric chemosensors assembled from naphthalimide dyes and crown ethers. *Phys. Chem. Chem. Phys.* **17**, 22749–22757. https://doi.org/10.1039/C5CP03510D (2015).
56. Yamamoto, Y. From σ- to π-electrophilic Lewis acids. Application to selective organic transformations. *J. Org. Chem.* **72**, 7817–7831. https://doi.org/10.1021/jo070579k (2007).
57. Kobayashi, S., Busujima, T. & Nagayama, S. A novel classification of Lewis acids on the basis of activity and selectivity. *Chem. A Eur. J.* **6**, 3491–3494 (2000).
58. Kobayashi, S., Nagayama, S. & Busujima, T. Lewis acid catalysts stable in water. Correlation between catalytic activity in water and hydrolysis constants and exchange rate constants for substitution of inner-sphere water ligands. *J. Am. Chem. Soc.* **120**, 8287–8288 (1998).
59. Frisch, M. J. et al. *Gaussian 09 Revision d. 01* (Gaussian Inc., 2009).

Acknowledgements

Authors thank the Latvia-Lithuania-Taiwan joint grant "Molecular Electronics in functionalized Purines: fundamental Study and applications (MEPS)" for the financial support. Funding received from the Research Council of Lithuania (LMT), project no. S-LLT-22-3.

Author contributions

K.B. data acquisition and analysis, design of the work; J.J. original draft preparation; J.J., G.J., S.J., I.N., M.T, H.T.C. idea & conceptualization, analysis, data interpretation, revise & editing; S.J., M.T. and H.T.C. supervision; G.K. software and simulation; A.B., Z.K., L.E.H., H.W.C. data acquisition and analysis.

Declarations

Competing interests

The authors declare no competing interests.

Additional information

Supplementary Information The online version contains supplementary material available at https://doi.org/10.1038/s41598-025-15262-8.

Correspondence and requests for materials should be addressed to J.J. or G.J.

Reprints and permissions information is available at www.nature.com/reprints.

Publisher's note Springer Nature remains neutral with regard to jurisdictional claims in published maps and institutional affiliations.